Applied Materials Today 28 (2022) 101528

Contents lists available at ScienceDirect

Applied Materials Today

journal homepage: www.elsevier.com/locate/apmt

Chlorine in NiO promotes electroreduction of CO_2 to formate

M.A. Rodriguez-Olguin [a], C. Flox [b,*], R. Ponce-Pérez [c], R. Lipin [d], F. Ruiz-Zepeda [e,f], J.P. Winczewski [a], T. Kallio [b], M. Vandichel [d], J. Guerrero-Sánchez [c], J.G.E. Gardeniers [a], N. Takeuchi [c,*], A. Susarrey-Arce [a,*]

[a] Mesoscale Chemical Systems, MESA+ Institute, University of Twente, PO. Box 217, Enschede AE 7500, the Netherlands
[b] Aalto University School of Chemical Engineering, Kemistintie 1, Espoo 02015, Finland
[c] Centro de Nanociencias y Nanotecnología, Universidad Nacional Autónoma de México, Carretera Tijuana-Ensenada km 107, Apdo., Ensenada, B.C. 22860, Mexico
[d] Department of Chemical Sciences and Bernal Institute, University of Limerick, Limerick V94 T9PX, Ireland
[e] Department of Materials Chemistry, National Institute of Chemistry, Hajdrihova 19, Ljubljana 1000, Slovenia
[f] Department of Physics and Chemistry of Materials, Institute of Metals and Technology, Lepi pot 11, Ljubljana, Slovenia

ARTICLE INFO

Keywords:
Halogens
Chlorine
NiO
CO_2 Reduction
Formate

ABSTRACT

We report the exceptional finding that NiO, a known electroactive catalyst for the reduction of CO_2 to CO, can be tuned to become an active electrocatalyst for CO_2 reduction to formate when chlorine is synthetically incorporated into NiO. The CO_2 reduction reaction (CO_2RR) is carried out on chlorine-containing NiO octahedral particles made by a solid-state synthesis method yielding a Faradaic efficiency (FE) of 70 % for formate production at -0.8 V vs. RHE with a partial current density of 14.7 mA/cm^2. XPS confirms the presence of Ni^{3+} and Ni^{2+} species, indicating the existence of uncoordinated Ni. The Ni^{3+}/Ni^{2+} ratio increases with the Cl concentrations on NiO. Cl concentrations are also confirmed with STEM-EDX. DFT modeling provides insights into the thermodynamic stability and CO_2RR mechanism over the Cl-containing NiO surface. It is suggested that Cl can occupy the defective sites created by oxygen vacancies on the NiO model with Cl (O-alpha+Cl). The surface Pourbaix diagrams constructed from DFT indicate the preferred surface terminations favorable at the operating conditions for the CO_2RR, which closely agrees with the experimental findings. The O-alpha+Cl has been found to promote CO_2RR to formate. Our results create new possibilities in the development of earth-abundant electrocatalysts for selective CO_2RR

1. Introduction

A significant part of the traditional energy value chains uses non-renewable fossil fuels as their primary raw material. These fuels are carbon-based, and their combustion releases carbon as CO_2 into the Earth's atmosphere. The increasing concentration of CO_2 in our atmosphere poses a threat to our living environment [1–3]. Capturing CO_2 in chemical bonds to make useful compounds is an excellent means of remediation [4]. Thereby, new alternatives for the chemical transformation of CO_2 can contribute to a low carbon climate-resilient future.

CO_2-recycling, such as the electrochemical conversion of CO_2, is an important technology that can effectively produce high-value chemicals using renewable sources. CO_2 can be activated at a catalyst surface upon adsorption, which, by subsequent proton and electron transfers, allows chemical transformations of CO_2 to carbon compounds, such as C_1 (e.g., CO, $HCOO^-$, CH_4) and C_2 (e.g., C_2H_4, alcohols) [5,6]. Among the C_1 and C_2 compounds, formate ($HCOO^-$) is of great interest due to its low toxicity and high H_2 carrier capacity (53.4g H_2/L) [7]. Metal and metal oxide catalysts (Bi, Cd, Co, Cu, Hg, In, Pd, Pb, Sn, and Zn) exhibit relatively good selectivity for formate at moderate overpotentials (**Table S1**). To our knowledge, there are no earlier reports on Cl-containing NiO electrocatalysts for electrocatalytic formate production (**Tables S1** and **S2**), demonstrating that the research on NiO electrocatalysts for formate production is still in its infancy. Compared to other approaches that directly use halides (I, Br, or Cl) in the electrolyte to reduce CO_2 [8], an ideal catalyst should contain halide species within its structure, as in the case of Cl. The effect of Cl has been showcased by increasing Cu stability during CO_2RR [9]. Another advantage is that Cl or other halogens in metals can selectively direct chemical pathways between the competitive processes (i.e., HER and CO_2R) [10–14].

* Corresponding authors.
E-mail addresses: crisflox@gmail.com (C. Flox), takeuchi@ens.cnyn.unam.mx (N. Takeuchi), a.susarreyarce@utwente.nl (A. Susarrey-Arce).

https://doi.org/10.1016/j.apmt.2022.101528
Received 22 February 2022; Received in revised form 9 May 2022; Accepted 16 May 2022
Available online 25 May 2022

Like Cu, NiO is an abundant earth catalyst for CO_2RR. Metallic or oxidized Ni is well-known for selectively producing CO during CO_2RR (**Table S2**) [15,16]. Apart from CO, the electrosynthesis of other chemicals such as formate, using Ni or NiO can extend the functionality of this environmentally friendly catalyst, especially compared to Bi or more expensive metals such as In, Pd, or Sn (**Table S1**). So far, the highest Faradaic efficiency to formate (FE_{HCOO-}) reported for the bare Ni electrocatalyst is around 22% at -0.7V vs. RHE, with a partial current density towards formate (J_{HCOO-}) of 0.24 mA/cm^2 [17–19]. More sophisticated systems, such as Ni nanoparticles over MnO_2, have achieved FE_{HCOO-} = 85% (at -0.85 V vs. RHE) at J_{HCOO-} = 7.2 mA/cm^2 [20]. However, more simple synthetic routes without additional support materials for evaluating the electrocatalytic performance of Ni (or NiO) should be assessed [21].

NiO is an attractive and unexplored option for the design of eco-friendly electrocatalysts (**Table S3**). A way forward is tuning the active sites on NiO. Although active site tunability is challenging, engineering NiO surface defects can aid in increasing the formate conversion and selectivity. Defect engineering concepts have been applied to NiO for catalytic reactions such as water splitting [22], hydrogen evolution [23], and recently CO_2 photoreduction [24]. It has been demonstrated that the electroactivity of NiO can be improved by increasing the number of defects in its structure [25–27]. To reach our aim of engineering defects in NiO, we considered a synthetic route based on electrospinning followed by multiple annealing steps as a potential direction to synthesize Cl-containing NiO. We have found that this approach leads to octahedral NiO crystallites. NiO octahedra have previously been produced using several synthetic routes [28–31]. It has been reported that there exists a relationship between the shape and the addition of halogen or organic ligands to the reaction medium, yielding to {111} faceted NiO [32]. Besides the preferential {111} facets [33–35], doping of NiO with low valence anions has been reported to increase the Ni^{3+}/Ni^{2+} ratio leading to the formation of non-stoichiometric nickel oxide. These non-stoichiometric species are uncoordinated species typically induced by defects in the electrocatalyst [5]. From this perspective, incorporating Cl into NiO during the synthesis would be an exciting approach for a high FE_{HCOO-} and J_{HCOO-} for NiO-based materials.

In this work, NiO is synthesized using a solid-state chemistry approach. As a preparation method, electrospinning of fiber materials is carried out using a $NiCl_2$-PVP precursor solution. The rationale behind the use of electrospinning is that it produces ca. 100 nm-size composite fibers that can act as a nucleation matrix for small and well-defined crystals of the desired Cl-containing NiO electrocatalyst after annealing in air. The functionality of Cl-containing NiO is then tested during CO_2RR. At 4 h, FE_{HCOO-} results in 70%, while for 24 h, the FE_{HCOO-} is 63% at -0.8 V vs. RHE with a J_{HCOO-} of ~ 13.7 mA/cm^2. In both cases, a small amount of CO with Faradaic efficiencies for CO (FE_{CO}) $\leq$ 3% and Faradaic efficiency for H_2 (FE_{H2}) = 15 % have been observed. The density-functional theory (DFT) modeling generates insight into the unexplored reaction mechanism during CO_2RR to formate over a Cl-containing NiO surface. The constructed model shows that the filling of oxygen alpha vacancies with Cl play an essential role during CO_2RR to formate. The defects can be correlated to non-stochiometric Ni^{3+} and Ni^{2+} species present in the Cl-containing NiO. XPS analysis demonstrated that the Ni^{3+}/Ni^{2+} ratio is proportional to the concentration of Cl. Cl concentrations have also been confirmed with STEM-EDX mapping. For the first time, the results confirm the high electrocatalytic activity of an environmentally friendly NiO electrocatalyst during CO_2RR to formate.

2. Methods

2.1. Synthesis of NiO octahedra

$NiCl_2$-PVP (polyvinylpyrrolidone) fibers were used as a precursor for NiO octahedral. The $NiCl_2$-PVP precursor solution was prepared by dissolving $NiCl_2.6H_2O$ (ACS grade, Sigma Aldrich) in ethanol (ACS grade, Alpha Aesar) until complete dissolution. Then, PVP (MW ~1,300,000 by LS, Sigma Aldrich) and N,N-Dimethylformamide (DMF, anhydrous, Sigma Aldrich) were added to the solutions and stirred magnetically overnight. The final concentrations were 0.22 M (as Ni), 8.09 mM (PVP), and 7.2 M (DMF). The $NiCl_2$-PVP solution was spun using a commercial electrospinning system from IME Technologies (The Netherlands) at 0.5 mL/h. The electrospinning was operated at 18 kV, using a stainless-steel needle of 0.4 mm inner diameter at a separation distance of 12 cm from the needle to the aluminum collector plate. The $NiCl_2$-PVP fibers were collected at 25 °C and relative humidity of 25%. After $NiCl_2$-PVP fiber deposition, the fibers were dried in a furnace at 80 °C for 12 h to remove the excess solvent.

The $NiCl_2$-PVP fibers were annealed (Nabertherm LH 15/12) in air, generating NiO octahedra. Two annealing steps were used. First, the fibers were annealed at 350 °C (ramp-up rate 0.5 °C/min) for 3 h to remove the organic components and then annealed at 550 °C (1 °C/min) for 1 h to generate crystalline NiO. The sample was named NiO@Cl-9%. Second, the NiO@Cl-9% sample was annealed at 550 °C (1 °C/min) for 1 h. The sample was then named NiO@Cl-1%. Third, the NiO@Cl-1% was annealed at 550 °C (1 °C/min) for 1 h to evaluate if Cl content varies over the next annealing steps. After annealing the NiO@Cl-1% sample, the Cl concentration remains similar to the untreated NiO@Cl-1%. In all cases, a controlled cooling ramp of 1 °C/min was used in both cases. It should be noted that during NiO@Cl-9% and NiO@Cl-1% preparation, the samples were pressed between two alumina plates (200 g in weight each). The rationale was to generate a compressed NiO fiber film to allow the formation of NiO octahedra.

The NiO drop-casting samples presented in the supporting information were prepared by directly pouring the $NiCl_2$-PVP electrospinning solution into porcelain crucibles and calcined at 550 °C (1 °C/min) for 1 h in air. NiO spin-coating samples from the supporting information were prepared using a Laurell WS-650-23 spin coater. The particles were prepared by pouring 1 mL of the $NiCl_2$-PVP electrospinning solution on top of thermally grown SiO_2 on Si wafers and using a spin force of 3000 rpm for 90 s and subsequently at 2300 rpm for 60 s. After spin-coating, the wafers were annealed at 550 °C (1 °C/min) for 1 h in air. Before spin coating, all SiO_2/Si wafers were cleaned with DI water and ethanol. Reduced NiO@Cl-9% (Ni@Red) was used for comparison. Ni@Red was prepared by reducing NiO@Cl-9% in H_2 (2% in N_2, gas flow: 50 cc/h) at 250 °C (5 °C/min) for 3.5 h.

2.2. Morphological characterization

2.2.1. HR-SEM

High-resolution scanning electron microscopy (HR-SEM) images of samples were taken using a Zeiss MERLIN SEM microscope operated at 2 kV coupled with High-Efficiency Secondary Electron Detector (HE-SE2). Samples NiO@Cl-9% and NiO@Cl-1% were analyzed on top of conductive carbon tape with no other preparation. To analyze the surface of the prepared NiO@Cl-9%-CNT-PVDF GDE electrode after 0 h, 4 h, and 24 h of electroreduction, the electrodes were washed first with MilliQ water to remove salts before analysis. After washing, the dry electrode was mounted on carbon tape with no further preparation. Energy dispersive X-ray (EDX) spectroscopy with a spatial resolution to nm range analysis was made using the detector incorporated with the HR-SEM.

2.2.2. STEM

Scanning transmission electron microscopy (STEM) was performed in a JEOL ARM 200 CF system operated at 80 kV. The estimated current density during imaging was 14.5 pA while using 68-175 mrad of the annular detector's inner and outer angles. The microscope is equipped with an SDD Jeol Centurio Energy-Dispersive X-ray spectrometer and a GIF Quantum (Gatan) Dual EELS (Electron Energy Loss Spectroscopy)

spectrometer. Samples for TEM were prepared by dispersing 5 mg of NiO@Cl-9% and NiO@Cl-1% samples in ethanol and sonicated for 5 min. The suspension was drop cast on Cu grids.

2.2.3. X-ray diffraction

The crystallographic phase of all samples was analyzed by X-ray powder diffraction (D2 PHASER, Bruker) using Cu Kα radiation (λ = 1.5418 Å) operated at 30 V, 10 mA, in a range between 10-85° 2θ, employing a step size of 0.05° and a scan speed of 0.1°/s. Si low background sample holder (Bruker) was used for the powder samples. Commercial NiO (Sigma-Aldrich) is used for comparison.

2.2.4. Chemical surface analysis

X-ray photoelectron spectroscopy (XPS) analysis was performed in a Quantera SXM machine from Physical Electronics using monochromated Al Kα (1486.6 eV). The samples were fixed on double-sided adhesive carbon tape mounted on a stainless-steel holder. Low energy electron flood gun was used to supply the missing photo- and Auger electrons. Low energy argon ions were used to remove the surplus of electrons by the electron flood gun. The electron binding energies were referenced to carbon C 1s at 284.8 eV. The collected core spectra were analyzed using the PHI Multipak V9.9.0.8 software (Physical Electronics, Inc.). High-resolution spectra were fitted using a Lorentzian-Gaussian line fitting and Shirley type to compensate for the background.

2.2.5. Raman measurements

Raman spectroscopy was used to identify the defects present in NiO@Cl-9% and NiO@Cl-1%. An Alpha300 R confocal Raman microscope/spectrometer (WITec, Germany) equipped with an MPlan FL N 100x/0.9 NA air objective (Olympus, Tokyo, Japan) was used. The samples were excited using an excitation laser of 532 nm operated at 5 mW power. The samples were prepared by dispersing 10 mg of a powder sample in one droplet of ethanol and drop-cast on top of glass slides.

2.3. Electrochemical characterization

2.3.1. Electrochemical flow cell

The CO_2RR was performed in an in-house designed microfluidic flow cell using a filter-press cell configuration. Working electrodes were prepared by spraying the as-prepared catalyst ink on the carbon gas diffusion layer (SIGRACELL 25BC) and dried at 80 °C overnight. The ink was prepared using 75% of carbon nanotubes and 25% of binder-catalyst (i.e., binder-NiO@Cl-9%). In this case, the binder composition was PVDF and Nafion 1:1. Then, the binder is mixed 1:1 ration with the catalyst. The final loading of NiO@Cl-9% was 1.25 mg/cm^2 (geometrical area 1.8 cm^2) in all cases studied. Platinum foil and an Ag/AgCl electrode were used as the counter and reference electrodes.

A previously activated cation exchange membrane (Nafion 115) was used between both compartments, and 0.1M $KHCO_3$ was used as the electrolyte on both sides, recirculated at 15 mL/min. Cyclic voltammetry (-1.1 to 0 V vs. RHE at 10 mV/s) was taken before and after each potentiostat experiment to know the catalyst's stability. The gas product detection was performed using gas chromatography analysis (490 Micro GC equipment from Agilent technologies) of gas sampled from the headspace during the electrolysis. The system was equipped with two channels - Molsieve 5 Å and the PoraPLOT - to analyze the following reaction products: hydrogen (H_2) and carbon monoxide (CO), methane (CH_4), ethane (C_2H_6), ethane (C_2H_4) as well as detection of CO_2. NiO-based catalyst produced H_2 and CO as main gas products, quantitatively detected in the Molsieve channel with 0.370 min and 1.642 min as retention times. The injector temperature was 110 °C, and the column temperature was set at 80 °C in both channels. The carrier gas was Ar at 200kPa and He at 150 kPa for Molsieve and PoraPLOT channels. Injections were sequentially performed every 5 min, being an injection time 30 ms. The calibration of the equipment for H_2 and CO was determined separately by injecting known quantities of pure gas. At the end of the bulk electrolysis, the catholyte was analyzed to quantify the liquid products by HPLC (AMinex column HPX-87X from Bio-Rad). The eluent used was 5 mM of H_2SO_4 with a 6 mL/min flow rate value at 60 °C. Typically, 10 mL of collected catholyte was mixed with 4M H_2SO_4 to decrease from pH 6.86 to pH 1–3, corresponding with formic acid formation. It should be noted that all current densities are expressed as cathodic currents. Thus a negative value is used in the manuscript. The Faradaic efficiency for the products was calculated according to the following equation:

$$\mathrm{FE}\ (\%) = \frac{(\mathrm{Nr})(\mathrm{n})(\mathrm{F})(\mathrm{V})}{\mathrm{Q}}$$

Nr is the number of electrons involved in obtaining the product *r* ($2e^-$ for the formate, CO and H_2), *n* corresponds to the number of *r* moles generated, *F* is the Faraday's constant (96,485 C/mol), and *Q* is the total charge passed during electrolysis.

2.3.2. Electrochemical surface area

The electrochemical surface area of the NiO@Cl-9% in supporting information was determined by determining the electrochemical double-layer capacitance by CV.

The double-layer capacitance (C_{dl}) measurement can be determined for all catalysts from the slope of the linear relationship between the current density obtained in the non-Faradaic region of the CVs at several scan rates. For that, the catalyst was immersed in 0.1 M $KHCO_3$, continuously purged with N_2, and CVs were obtained at scan rates within the range from 5 mV s^{-1} to 80 mV s^{-1}.

2.4. Mechanistic insights with density-functional theory

2.4.1. First-principles calculations

We have investigated the CO_2 reduction with and without Cl atoms using non-collinear spin-polarization first-principles total-energy calculations. Although the NiO nanoparticles show different facets, SEM and TEM images have shown that the most common is the (111) termination. Therefore, we have used the NiO(111) surface to model the CO_2 reduction reaction. Total energy calculations were performed in the Density Functional Theory (DFT) framework as implemented in the Vienna Ab initio Simulation Package (VASP) [36–39]. Exchange-correlation energies have been treated according to the generalized gradient approximation (GGA) with the Perdew-Burke-Ernzerhof (PBE) parameterization [40]. Also, since Ni has d-orbitals with highly correlated electrons, we have included the Hubbard correction (GGA+U) [41]. Previous reports have demonstrated that a value of U = 6.3 and J = 1 eV describes the NiO physical properties very well [42,43]. Therefore, we have used these values in our calculations. The electronic states have been expanded using the projector-augmented wave basis (PAW) [44,45] with an energy cutoff of 425 eV. Van der Waals (VdW) forces have been considered using the Grimme-D3 correction [46,47]. The NiO(111) surface has been simulated employing the supercell method with a 2 × 2 periodicity. Each supercell was formed by a slab and a vacuum space larger than 20 Å to avoid interactions between adjacent slabs; the slab was constructed with 9 atomic layers, where the lower layers were frozen in their ideal positions to simulate the bulk-like environment. In optimizing the geometries, we have required all forces to be less than 0.01 eV/Å and energy differences less than 1×10^{-4} eV. Integration of electronic states in the Brillouin zone has been performed using a Monkhorst-Pack mesh of 5 × 5 × 1 k-points [48].

2.4.2. Surface formation energy formalism

In order to investigate the stability of different surface terminations with different numbers of atoms and chemical species, we have used the Surface Formation Energy (SFE) formalism adapted to our system, following Refs. [49–53]. In the SFE formalism, we consider thermodynamic equilibrium between the surface and the bulk:

$$\mu_{Ni}^{bulk} + \mu_{O}^{mol} - \Delta H_f = \mu_{NiO}^{bulk} = \mu_{Ni} + \mu_{O}$$

with

$$\mu_{Ni}^{bulk} \leq \mu_{Ni}$$

and

$$\mu_{O}^{mol} \leq \mu_{O}$$

Where μ_i is the chemical potential of the ith atomic specie, and ΔH_f is the enthalpy of formation. Our calculated value of ΔH_f is 3.01 eV in good agreement with previous reports [8]. We can write the surface formation energy as follows:

$$E_f = E^{slab} - E^{ref} - \sum \Delta n_i \mu_i$$

Where, E^{slab} is the total electronic energy of the system, and n_i is the number of atoms of the ith species, E^{ref} is the total energy of an arbitrary reference, which in this case is the ideal Ni-terminated surface, and Δn_i is the excess or deficit of atoms of the ith species in comparison with the reference. We plot the SFE as a function of the chemical potential from O-rich conditions ($\mu_O = \mu_O^{mol}$) and ($\mu_{Ni} = \mu_{NiO}^{bulk} - \mu_{Ni}^{bulk}$) to Ni-rich conditions ($\mu_{Ni} = \mu_{Ni}^{bulk}$) and ($\mu_O = \mu_{NiO}^{bulk} - \mu_O^{mol}$). According to our formalism, the most stable surfaces have lower formation energies.

2.4.3. Surface Pourbaix diagram

The thermodynamic stability of the NiO(111) model upon hydrogenation can be described by surface Pourbaix diagrams, which are constructed at the relevant U_{SHE} (Standard Hydrogen Electrode at pH=0, P_{H2} =1 bar, T=300 K) and pH for the stable surfaces. For the study, adsorption of up to 1ML of H atoms on the O-alpha and O-alpha+Cl surfaces is considered. The hydrogens are adsorbed consecutively on the surfaces as given below:

$$\frac{x}{2}H_2 + * \rightarrow xH^*$$

Where * represents the adsorbent while x represents the number of hydrogens adsorbed on the NiO(111) model system.

At constant potential and pH, change in free energy of hydrogenation reaction on various absorbate configurations as a function of the number of H atoms adsorbed (n), is given by:

$$\Delta G = nU_{SHE} + nk_B TpH + \Delta G_{H^*} - G^* - \frac{1}{2}nG_{H_2}TpH$$

Where ΔG_{H^*} and G^*denote the change in Gibbs free energy upon adsorption of hydrogen on the surface and free energy of the adsorbed state, respectively. ΔG_{H^*} can be further written as follows:

$$\Delta G_{H^*} \approx \Delta E_{H^*} + \Delta F_{vib}$$

Here, ΔE_{H^*} represents the electronic energy difference while F_{vib} is the Helmholtz vibrational energy which can be calculated based on the zero-point vibrational energy contribution $E_{H^*,ZPE}$ and the vibrational entropy S_{vib}:

$$F_{vib} = E_{H^*,ZPE} - T.S_{vib} = \frac{1}{2}\sum_i \left\{ h\nu_i + 2k_B T ln\left[1 - \left(-\frac{h\nu_i}{k_B T}\right)\right]\right\}$$

Where ν_i represents the wavenumbers obtained from the vibrational frequencies of hydrogen atom(s) over the surface.

3. Results and discussions

3.1. Preparation, morphology, and composition of electrocatalysts

Electrospinning is extensively used to produce nanofibers of different materials, but in this work, it is employed as a deposition method of $NiCl_2$-PVP nanofibers (**Fig. S1**). The $NiCl_2$-PVP nanofibers are used as precursors for the solid-state synthesis of Cl-containing NiO. The final shape of the NiO depends strongly on the deposition method (**Fig. S2**). Electrospinning results in the most suitable deposition route for the formation of NiO octahedral crystallites (Fig. 1**a**) when compared with drop casting or spin coating, for which octahedral crystals are not formed (**Fig. S2**). We propose that the formation of the NiO octahedra Cl-containing named NiO@Cl-9% (i.e., NiO with 9%at of Cl) is achieved via the coalescence of $NiCl_2$-PVP nanofibers (**Fig. S1**). $NiCl_2$-PVP nucleates at 550 °C with Cl and PVP acting as ligands, yielding octahedral particles. Under the same conditions, a second thermal treatment is applied to the NiO@Cl-9% leading to the catalyst named NiO@Cl-1% (i.e., NiO with 1at% of Cl) in Fig. 1**d**. Morphological analysis for NiO@Cl-9% and NiO@Cl-1% can be seen in Fig. 1**a** and **d**. The images show the formation of polydisperse NiO octahedra with edge sizes of 1.7 ± 0.6 μm. Morphological variations of NiO@Cl-1% are evidenced in Fig. 1**d**. Most NiO@Cl-1% octahedral crystals show heavy grooves that originated during the second thermal treatment, most probably due to the removal of Cl. Our hypothesis is compared with other synthetic approaches where the decomposition of the precursors leads to defective NiO crystals [54]. It should be noted that changes in NiO morphology might be expected at higher temperatures than 550 °C [55].

A closer inspection with STEM bright-field (BF) at the surface of the crystallites from NiO@Cl-9% and NiO@Cl-1% is shown in Fig. 1**b** and **e**. The relatively low magnification STEM images show a side view of the octahedral crystallites. A significant number of steps and grooves over the NiO@Cl-1% surface (Fig. 1**e**) caused by the thermal treatment can be seen. Even though it is possible to find smaller crystals with similar features and roughness in NiO@Cl-9% (Fig. 1**a**), most of the roughness in NiO@Cl-1% is found prominently over average size crystals (Fig. 1**d**). Similarly, it is possible to find flat facet octahedra in NiO@Cl-1%, although they are very rare and of small dimensions. In Fig. 1**c**, the high resolution (HR)-STEM annular dark field (ADF) image for NiO@Cl-9% shows part of the edge of the crystal oriented along [101] with lattice planes of spacing 2.3 Å and 2.1 Å that correspond to the (111) and (020) crystallographic planes of the face-centered cubic structure of NiO. [56] This agrees with the crystallographic characteristics of NiO shown in the XRD results displayed in **Fig. S3a**.

The Cl amount in NiO@Cl-9% and NiO@Cl-1% bulk samples is semi-quantified considering Ni and Cl ratio in SEM-EDX and STEM-EDX. Both methods give similar Cl relative content; therefore, in Table 1, we only display the Cl relative content for NiO@Cl-9% and NiO@Cl-1% as analyzed from STEM-EDX. A 2-fold reduction in Cl atomic concentration is observed for NiO@Cl-1%. The result confirms that part of the Cl is removed during the annealing of the NiO@Cl-9% sample. The Cl-distribution over the NiO octahedra can be appreciated in the STEM-EDX mappings of NiO@Cl-9% and NiO@Cl-1%, displayed in Fig. 1**f–i** and **j–m**. As can be observed, Cl is distributed mostly over the NiO crystallites, although with a significant reduction in the case of NiO@Cl-1%. A yellow arrow in Fig. 1**j** highlights the roughness observed in the NiO@Cl-1% surface.

The chemical composition of NiO@Cl-9% and NiO@Cl-1% is investigated with XPS to understand the role of Cl in NiO. High-resolution XPS spectra and the corresponding fitted curves for NiO@Cl-9% (top panel) and NiO@Cl-1% (bottom panel) are presented in Fig. 2. The XPS spectra correspond to (**a**) Ni 2p, (**b**) O 1s, and (**c**) Cl 2p. In Fig. 2**a**, the observed binding energies for Ni $2p_{3/2}$ are 854.0 eV and 853.9 eV for NiO@Cl-9% and NiO@Cl-1%, corresponding to lattice Ni^{2+} in NiO [57, 58]. Ni^{3+} species are found in NiO@Cl-9% and NiO@Cl-1%, with binding energy at 855.8 and 855.6 eV attributed to uncoordinated Ni, most probably from defective NiO. Similar binding energies for Ni^{3+} in Ni_2O_3 or NiOOH could be expected [59–62]. The corresponding Ni $2p_{1/2}$ split-orbit peaks appear at + 17.5 eV from Ni $2p_{3/2}$ signal. The results agree with NiO-based materials using similar precursors (i.e., $NiCl_2$) and other synthetic approaches [63,64]. Raman measurements also confirm Ni^{2+} and Ni^{3+} species in NiO (**Fig. S5**).

The fitted peaks for Ni^{2+} and Ni^{3+} within the 850-860 eV region for

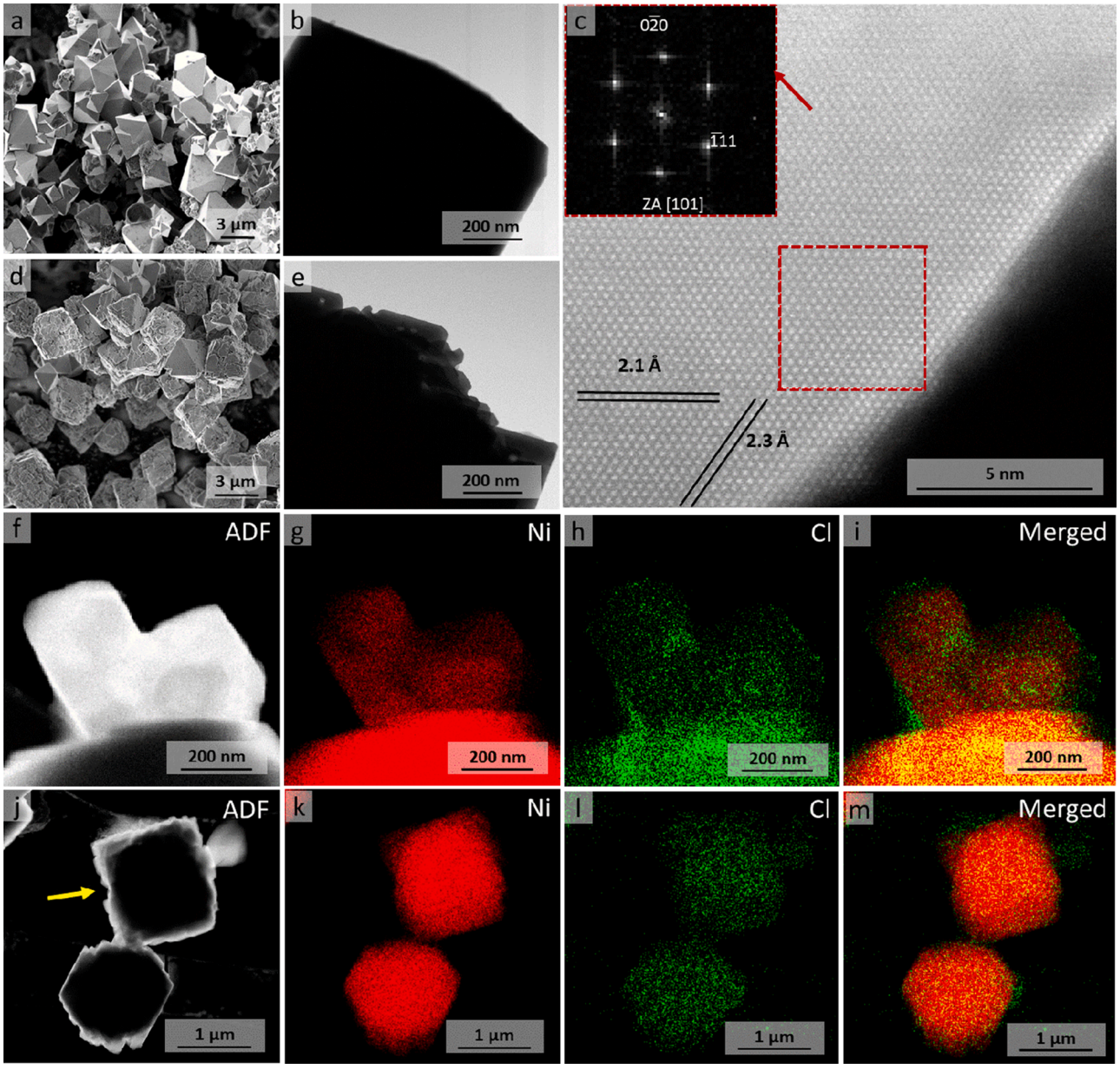

Fig. 1. NiO@Cl-9%: (a) SEM image showing crystallites with flat octahedral morphology, (b) STEM BF side view of one of the crystallites with flat facets, and (c) high-resolution STEM ADF image of a NiO crystal edge. The red dashed box indicates the location of the processed fast fourier transform (FFT) inset, which exhibits lattice planes and the zone axis of the oriented NiO crystal. The spaced solid black lines on the image represent the measured interplanar distances. NiO@Cl-1%: (d) SEM image of crystallites with an octahedral shape, however displaying signs of surface roughness, (e) STEM BF side view of a crystallite surface having grooves and irregular topography. (f-i) and (j-m) STEM-ADF and STEM-EDX maps of NiO@Cl-9% and NiO@Cl-1%, respectively. Ni signal in red, (h,l), Cl signal in green, and (i,m) overlay of Ni and Cl signals. The O signal can be found in **Fig. S4**. The arrow in (j) illustrates the features of roughness observed in the SEM images.

Table 1
Cl content (at%) for NiO@Cl-9% and NiO@Cl-1%, as estimated with STEM-EDX. Relative Cl content (at%) determined with XPS for NiO@Cl-9% and NiO@Cl-1%. Ni^{3+}/Ni^{2+} ratio determined with XPS for NiO@Cl-9% and NiO@Cl-1%.

	STEM-EDX Cl content (at%)	**XPS**	**XPS Ni^{3+}/Ni^{2+}**
NiO@Cl-9%	1.2	9	4.6
NiO@Cl-1%	0.7	1.5	1.2

NiO@Cl-9% and NiO@Cl-1% are integrated for comparison. The ratio between the integrated values is presented in Table 1. It is clear from this table that NiO@Cl-9% has the highest amount of Ni^{3+} species with a Ni^{3+}/Ni^{2+} ratio of 4.6. In the case of NiO@Cl-1%, Ni^{3+}/Ni^{2+} is close to 1.2, indicating a lower amount of Ni^{3+} species in NiO. A more detailed analysis to explain the relation between Ni^{3+} and Cl is discussed in the DFT section. Fig. 2**b** shows the XPS spectra and fitted curves for O 1s. The O 1s peaks at binding energies of 529.4 and 529.3 eV for NiO@Cl-9% and NiO@Cl-1% are assigned to oxygen in the NiO lattice [65]. The O 1s peaks at 531 eV label as Ni-O for NiO@Cl-9% and NiO@Cl-1% are associated with Ni-OH, Ni_2O_3, or non-stoichiometric NiO, probably from oxygen defects [66–69]. The O 1s peak at 532.2eV for NiO@Cl-1% corresponds to surface OH^- groups, which has been observed before for NiO [59,66–69]. The remaining O 1s signal at 532.9eV for NiO@Cl-9% is assigned to C-O species [59,70]. No nitrogen is detected in all cases, indicating that PVP has been decomposed to oxidized carbon species (**Fig. S6**) with a total carbon content of 14 at% in NiO@Cl-9% and NiO@Cl-1%. No graphitic carbon has been found, as shown in **Figs. S5**

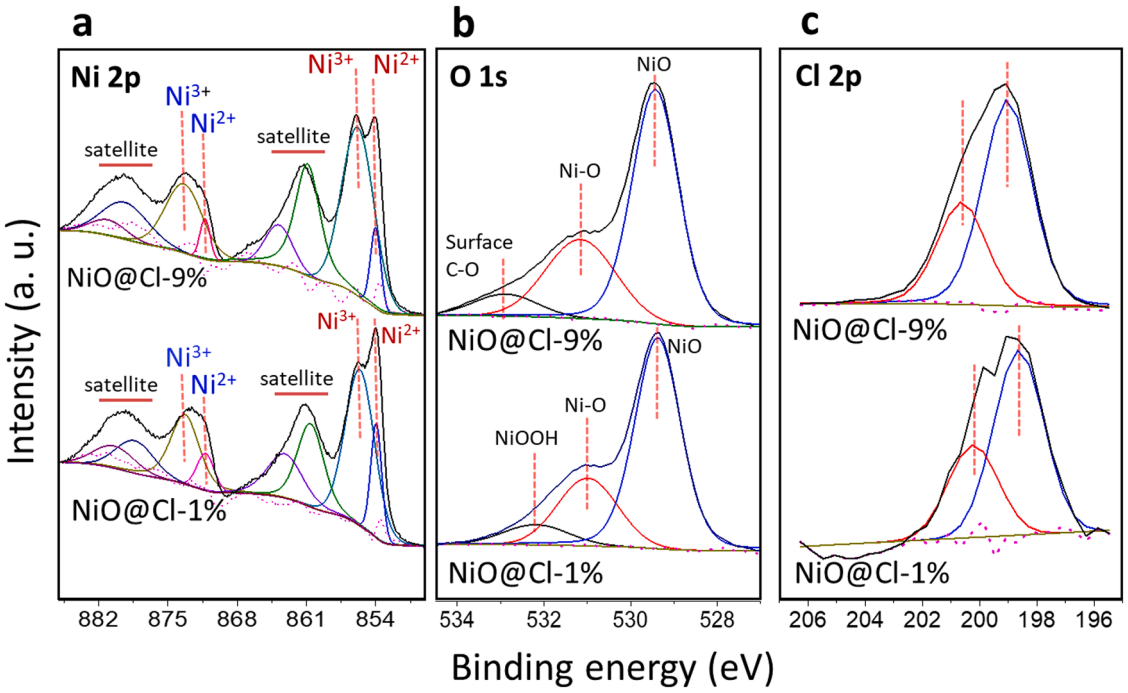

Fig. 2. XPS spectra for NiO@Cl-9% (top panel), NiO@Cl-1% (bottom panel). XPS spectra recorded for (a) Ni 2p, (b) O 1s, and (c) Cl 2p.

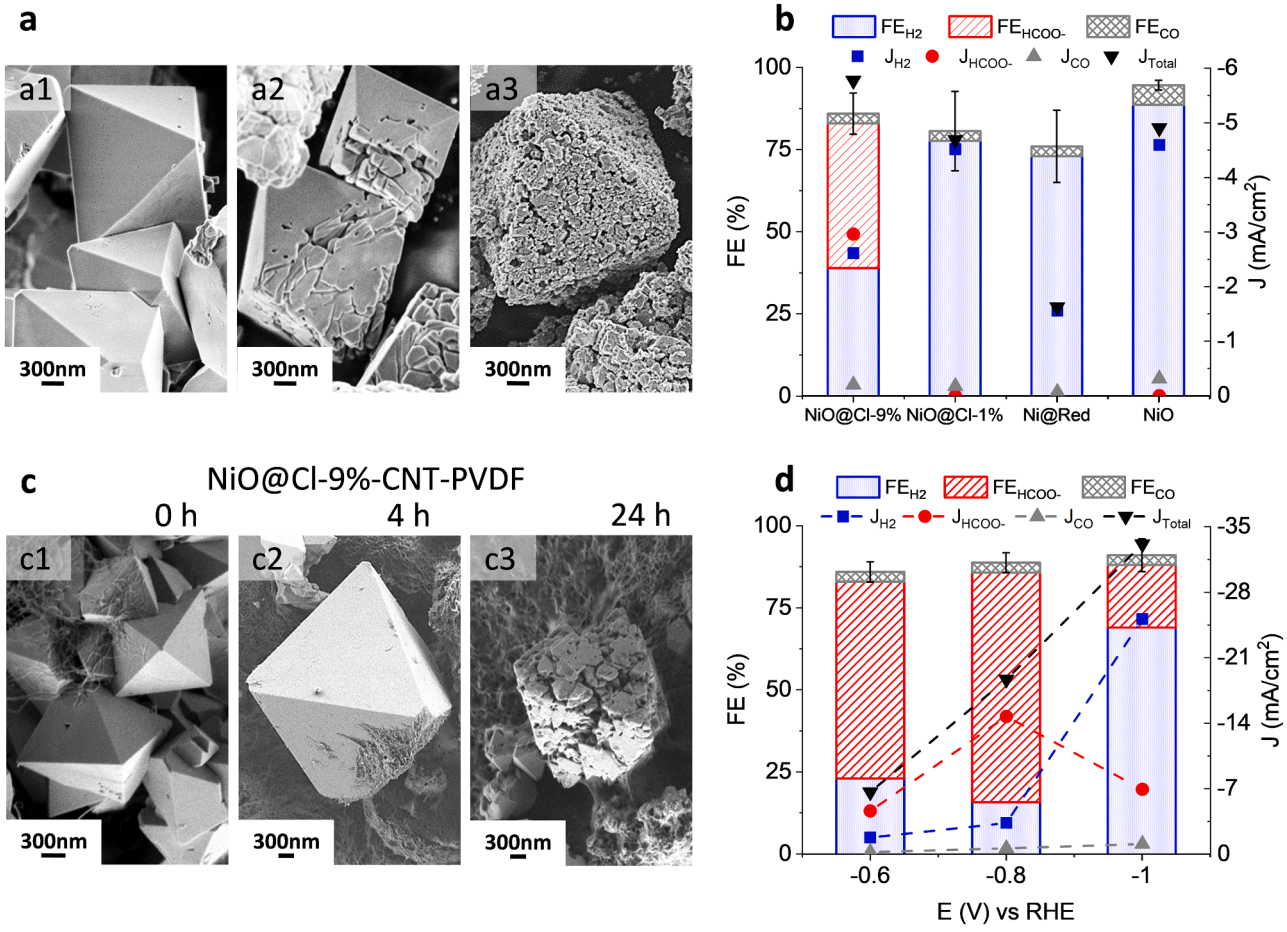

Fig. 3. (a) SEM images of (a1) NiO@Cl-9%, (a2) NiO@Cl-1%, and (a3) Ni@Red. (b) FE and partial current densities after 4 h at -0.8 V for NiO@Cl-9%, NiO@Cl-1%, Ni@Red, and NiO with CNT sprayed over GDE. (c) SEM images of NiO@Cl-9%-CNT electrodes with PVDF: (c1) as prepared, (c2) after 4 h, and (c3) after 24 h of electroreduction. (d) FEs and partial current densities of NiO@Cl-9%-CNT-PVDF-GDE for H_2 (4 h), CO (4 h), and $HCOO^-$ (4 h) at -0.6, -0.8, and -1.0 V. Note that during CO_2R, the pH of the bulk electrolyte remained at 6.8.

and **S6**. Additionally, Na (0.6 at%) and Ca (0.5 at%) have been found in this set of samples. The XPS Cl $2p_{3/2}$ spectra and fitted peaks are presented in Fig. 2**c**. The peaks at 199.1 eV (NiO@Cl-9%) and 198.6 eV (NiO@Cl-1%) are typically associated with chlorine [67,71]. The low binding energy value for NiO@Cl-1% could indicate an increased electron density due to the Cl loss [67,71,72]. The peak located around 201 eV is likely related to the presence of Cl-organic bonds [73].

3.2. Evaluation of formate production via electrochemical CO_2RR

The functionality of the NiO@Cl-9% is investigated during the CO_2RR to formate. NiO@Cl-1%, reduced Ni (Ni@Red), and commercial NiO (NiO) are used as controls to generate insights into the formate formation mechanisms in NiO@Cl-9%. Fig. 3**a** shows a high resolution (HR)-SEM image of the NiO@Cl-9% (Fig. 3**a1**), NiO@Cl-1% (Fig. 3**a2**), and Ni@Red (Fig. 3**a**). SEM-EDX for NiO is shown in **Fig. S7**. No Cl is observed for the commercial NiO. The Faradaic Efficiencies (FE) and partial current densities of the different reduction products are presented in Fig. 3**b**. For these experiments, 1.2 mg/cm^2 of the NiO@Cl-9%, NiO@Cl-1%, Ni@Red, and NiO catalyst is mixed with carbon nanotubes (CNT) and sprayed over a gas-diffusion electrode (GDE) to overcome CO_2 mass transport issues during CO_2RR [74]. Each prepared GDE is mounted in a continuous flow electrochemical cell in 0.1M $KHCO_3$ connected to an online gas chromatograph (GC) to analyze the gas products and *ex-situ* HPLC to analyze the liquid products.

In Fig. 3**b**, continuous flow electrochemical measurements under constant voltage have been assessed using various potentials (-0.6, -0.8, and -1.0 V (vs. RHE)). The rationale behind these potentials is that above -0.6 V vs. RHE, hydrogen evolution reaction or CO_2R seems to occur (**Fig. S8**). For simplicity, -0.8 V (vs. RHE) is presented in Fig. 3**b**. Here, the highest J_{HCOO^-} is found for NiO@Cl-9%. The NiO@Cl-9% shows J_{HCOO^-} of 2.9, J_{H2} of 2.6, and J_{CO} of 0.2 mA/cm^2 (see a closed: red circle, blue rectangle, and up gray triangle). For NiO@Cl-1%, the J_{H2} is 4.5, and 0.17 mA/cm^2 for J_{CO}. Followed by Ni@Red with J_{H2} = 1.5, and J_{CO} = 0.1 mA/cm^2. Control experiment using NiO, shows a J_{H2} = 4.6, and J_{CO} = 0.3 mA/cm^2. The FE_{HCOO^-} for NiO@Cl-9% is 44% (Fig. 3**b**), while the FE_{H2} reaches 39%. Additionally, FE_{CO} for NiO@Cl-9% is close to 3%. Similar FE_{CO} have also been found for NiO@Cl-1% and Ni@Red. Besides FE_{CO}, the only additional product obtained for NiO@Cl-1% and Ni@Red is hydrogen, achieving FE_{H2} = 78% and FE_{H2} = 73%, respectively. This might be related to Cl content. NiO@Cl-1% and Ni@Red have a ca. 1.5 at% Cl and a ca. 1.7 at% Cl (estimated by XPS). For the NiO used as control, FE_{H2} = 88.6% and FE_{CO} = 6% are observed. For NiO, no Cl has been found by SEM-EDX in **Fig. S7**. Overall, the total FEs (FE_T) obtained in Fig. 3**b** are 86% for NiO@Cl-9%, 81% for NiO@Cl-1%, 76% for Ni@Red, and 94.6% for commercial NiO.

The FE_{HCOO^-} is increased further by incorporating polyvinylidene fluoride (PVDF) into the NiO@Cl-9% GDE (i.e., NiO@Cl-9%-CNT-PVDF), as presented in Fig. 3**c** and **d**. The rationale behind PVDF is that it can act as a blocking proton agent, which affects the proton availability and proton transfer rates [75]. In Fig. 3**c1**, an SEM image of pristine NiO@Cl-9%-CNT-PVDF is included, indicating no changes in the morphology of NiO@Cl-9% on CNT-PVDF. An SEM of the NiO@Cl-9%-CNT-PVDF electrode is shown after 4 h of electroreduction at -0.8 V (Fig. 3**c2**). No changes in morphology are found. Chronoamperometry of NiO@Cl-9%-CNT-PVDF is also performed to demonstrate the NiO stability in **Fig. S9**.

The partial current densities displayed in Fig. 3**d** show at -0.6 V, a J_{HCOO^-} of -4.6 mA/cm^2, J_{H2} of -1.8 mA/cm^2, and J_{CO} of -0.2 mA/cm^2 achieving a total current density (J_T) of -6.6 mA/cm^2. At -0.8 V, the J_{HCOO^-} is -14.7, J_{H2} is -3.3, and J_{CO} is -0.6 mA/cm^2 with a J_T of -18.6 mA/cm^2. Finally, at -1.0 V, the J_{HCOO^-} is -6.9 mA/cm^2, J_{H2} is -25.1 and J_{CO} is -1 mA/cm^2, and J_T of -33.3 mA/cm^2. The results demonstrate that J_{HCOO^-} reaches a maximum when a potential of -0.8 V vs. RHE is applied. Low potentials may not provide enough energy for the reaction to proceed since we see an increase in J_{HCOO^-} at -0.8 V. When the potential exceeds -0.8 V, the hydrogen evolution reaction (HER) is preferred [65], decreasing the number of available sites to transform CO_2 in $HCOO^-$. The results align with the observations in Fig. 3**b** and cyclic voltammetry measurements for NiO@Cl-9%-CNT-PVDF in **Fig. S8**. For CO, the production remains similar between the various applied potentials, such as -0.8V in Fig. 3**d**. From these results, we can say that the potential window for formate is relatively small compared to Sn (**Table S1**). However, our results widen the applicability of NiO towards formate, with the advantage of NiO being less costly than Sn and more environmentally friendly than Bi (**Tables S1** and **S2**). To this end, when comparing the total FE (FE_T) for the various applied potentials, -1.0 V remains the highest with 91.0%. Other FE_T are 88% (-0.8 V) and 86% (-0.6 V).

Since we aim to demonstrate the functionality of NiO@Cl to produce $HCOO^-$, hereafter, the main emphasis is on the synthesized NiO@Cl-9% catalyst, which achieved the highest FE_{HCOO^-} (ca. 70%) at -0.8 V. Focusing now on the electrochemical results from NiO@Cl-9% in Fig. 3**b** and **d**, it is evident that the highest FE_{HCOO^-} and J_{HCOO^-} is found when PVDF is present. The results agree with previous studies, where PVDF acts as a blocking proton agent, which could affect the proton availability and proton transfer rates, stabilizing the CO_2 intermediates [75]. It is important to mention that the presence of PVDF does not change the electrochemical surface area (ECSA) as the NiO@Cl-9%-CNT-PVDF reveals similar C_{dl} for NiO@Cl-9% and NiO@Cl-9%-CNT-PVDF in **Fig. S10** and **Table S4**.

Finally, the long-term stability of NiO@Cl-9%-CNT-PVDF is investigated for 24 h at -0.8 V (**Fig. S11**). The FE_T remains close to 90% at a J_T = 21 mA/cm^2. FE_{HCOO^-} reveals an 8% reduction, i.e. FE_{HCOO^-} = 63% with a J_{HCOO^-} = 13.3 mA/cm^2. FE and partial current densities for H_2 and CO have been found close to FE_{H2} = 20% with a J_{H2} = 4.2 mA/cm^2, and FE_{CO} = 6.5% with a J_{CO} = 1.3 mA/cm^2 after 24 h. Morphological analysis with SEM is carried out to corroborate possible morphological changes in the NiO@Cl-9%-CNT-PVDF GDE after 24 h exposure to electroreduction (Fig. 3**c3**). It is observed that the NiO octahedra are etched. For comparison, SEM of NiO octahedra as-sprayed over the GDE and after 4 h of operation are presented in Fig. 3**c1, c2**. This observation indicates that variations in morphology can be attributed to the reduction of NiO to Ni and the loss of Cl during CO_2RR [76]. Loss of Cl in Fig. 3**c3** could lead to similar structural changes as in NiO@Cl-1%. (Fig. 3**a2**). Loss of Cl might also affect the presence of Ni^{3+}, similar to either NiO@Cl-1% (Table 1) or Ni@Red (**Fig. S12**). It should be noted that Cl losses are complicated to measure in solution at such low catalyst concentrations. However, structural analysis before (Figs. 3 and **S13**) and after 24 h reaction (**Figs. S14**–**S16**) provide insights into morphological changes after CO_2RR. The comparison reveals that NiO morphology is affected when applying a cathodic potential. The Cl concentration in NiO remains close to 0.4 at% after 24h (**Fig. S15**). The results evidence a lower Cl concentration, approximately 0.3 at%, than the electrode at 0h (Table 1 and Fig. 3**c**). XRD analysis does not exhibit structural changes between 0 h and 24 h (**Fig. S3**).

The reduction of the catalyst is demonstrated with XPS (**Fig. S12**). Although the Ni@Red (Fig. 3**a3**) has been exposed to air after its reduction in H_2, it is fair to say that it retains features from reduced Ni. The results indicate that surface species greatly affect the electroreduction of CO_2. Ni^{2+} and reduced Ni species profoundly affect FE_{HCOO^-} (Fig. 3**b**). Therefore it is important to understand the type of active site in NiO@Cl-9%. XPS analysis of $NiCl_2$ and $Ni(ClO_4)_2$ generates insights on the surface species on NiO@Cl-9% (**Fig. S17**). $NiCl_2$ is the main precursor of the NiO@Cl-9% octahedra, and $Ni(ClO_4)_2$ discriminates between NiCl or NiOCl species on the NiO catalyst. **Fig. S16** suggests that Cl is not coordinated as in $Ni(ClO_4)_2$, and it has more similarities with $NiCl_2$. More evidence is provided in **Figs. S18** and **S19**. In **Fig. S18**, the EELS signal shows the presence of Cl at the surface of the NiO crystallites. In **Fig. S19**, the Ni L23 edge is used to obtain the L3/L2 ratio and determine the chemical environment of Ni-species in $NiCl_2$, NiO@Cl-9%, and NiO@Cl-1%. The measurement shows that for NiO@Cl-9%, more points have a lower L3/L2 ratio relative to Ni^{2+},

indicating a higher fraction of Ni^{3+} than NiO@Cl-1%. Note that $NiCl_2$ is used as a reference for the determination of Ni^{+2} . Furthermore, electrodes at 0 h and after 24 h of electroreduction from Fig. 3**c** are analyzed with XPS in **Fig. S20**. The Ni 3p is used because the Ni 2p overlaps with the F Auger lines of the PVDF. The XPS analysis for Ni 3p confirms the presence of Ni^{2+} and Ni^{3+} species before and after CO_2RR (Fig. 3**c**). A shift to lower binding energy has also been observed in **Fig. S20**. The shift to lower binding energy might indicate the loss of Cl. Alternatively, the results indicate the reduction of the NiO due to the applied cathodic potential, which can explain the morphological changes in Fig. 3**c**. We do not discard the possibility that the produced H_2 might also reduce NiO to Ni during the application of the cathodic potential [77]. However, considering Faraday law, FE losses due to NiO reduction are estimated to be close to 4% or lower. These losses have not been taken into account in Figs. 3 and **S11**. Our findings indicate that Cl species can be allocated in defects, such as oxygen vacancies forming three-fold coordination with Ni in the NiO (Fig. 4).

3.3. *Modeling of the electrocatalyst surface, thermodynamics, and CO_2RR mechanism*

To gain mechanistic insights on how Cl-containing NiO surfaces promote CO_2 reduction to formate, spin-polarized DFT calculations are carried out. The model accounts for defects present in the NiO (111). The surface formation energy (SFE) for various NiO (111) surfaces is assessed using DFT (Figs. 4 and **S21**). SFE plots are shown as a function of the chemical potential in a range of chemical potentials varying from -3.0 eV (O-rich conditions) to 0.0 eV (Ni-rich conditions) structures (Fig. 4**a**). It should be noted that Fig. 4 shows the most stable surface terminations considered. Other NiO surface terminations studied are presented in **Fig. S21**. From Fig. 4**a, b**, it can be seen that the only stable structures are the ones with a vacancy (O-alpha model) [78] under oxygen-rich conditions and the octopolar reconstruction (which is formed by a pyramidal-like structure) at intermediated and Ni-rich conditions. [79] Since we are dealing with an environment rich in oxygen, the NiO surfaces are modeled using the O-alpha model. We show the electrostatic potential isosurfaces (EPIs) of the NiO surfaces with and without Cl to demonstrate the reactivity created by Cl substitution of surface hydroxyl groups in **Fig. S22**. Moreover, the addition of water to the surface should lead to the vacancy configuration for the octopolar reconstruction. Surfaces with vacancies are very reactive, and when Cl interacts with the vacancy is adsorbed on it, forming three-fold coordination with Ni (2 × 2-O alpha + Cl model), which is stable at O-rich and intermediated conditions (gray line) (Fig. 4**a** and **c**) over extended pH ranges (Fig. 5). Previous work from Xu et al. has shown that Ni vacancies in a NiO bulk structure result in the presence of Ni^{3+} [59]. We investigated in detail the possible relationship between the presence of Cl and the amount of Ni^{3+} in the structure through the Bader charge analysis [80]. We calculated the Bader charge in pristine NiO bulk as a reference. Our calculations show that the Ni donates 1.28 e to its neighbor O atoms. When a Ni vacancy is present, its neighbor Ni atoms donate 1.37 e to their neighboring O atoms, just as in the case reported in [59]. As previously demonstrated, Cl atoms adsorb on the O vacancy sites. Therefore, when higher Cl content exists on the samples, more NiO-terminating O and OH sites will actually be substituted with Cl. However, increasing the number of O vacancies also requires the presence of Ni vacancies in the octopolar structure. We have calculated the Bader charges of a Cl-covered O-alpha and a Cl-covered O-alpha with a Ni vacancy at different sites. A Ni vacancy is more stable in the third layer than on the surface. The charge donated by the Ni atoms close to Cl and close to the Ni vacancies are 1.25 e and 1.35 e, respectively, showing that Ni vacancies drive Ni^{3+} species. Calculations have also been performed for the octopolar structure, finding similar results: the vacancy becomes more stable at inner layers, and Ni atoms close to it donate more charge (Ni^{3+} is observed around the Ni vacancy). These results explain the increase of the Ni^{3+}/Ni^{2+} ratio at the surface structures with higher Cl content.

Surface Pourbaix diagrams shown in Fig. 5 are constructed to assess the thermodynamic stability of favorable surfaces with hydrogen adsorbed as a function of pH and potential [81,82]. In this case, the O-alpha and O-alpha with a chlorine atom on the vacant site (O-alpha+Cl) are chosen because they result in the most stable surface in SFE plot in Fig. 4. The O-alpha without Cl is assessed first. The thermally stable surfaces on the defective O-alpha structure upon adsorption of H atoms at different coverages are shown in Fig. 5 as a function of pH and potential. The H coverage is defined as the number of hydrogen atoms adsorbed per total number of surface oxygen atoms. The Pourbaix diagram shows three terminations to be most favorable in the potential range of -1 to 2.5 V. At potentials over 2.05 V and low pH, the O-alpha surface without the H atoms is found to be stable. The formation of 0.33ML of H atoms is likely from 2.05 to 1.34 V. A large potential range of 0.51 to -1 V favors complete coverage of H atoms over the oxygens in the first layer, as shown in Fig. 5**a**. On moving to an alkaline medium (pH=14), with a slope of -59 meV per change in pH of 1, these three favourable terminations occur at lower potential ranges. It must be noted that the structure with 1.00 ML of H atoms falls over the potential

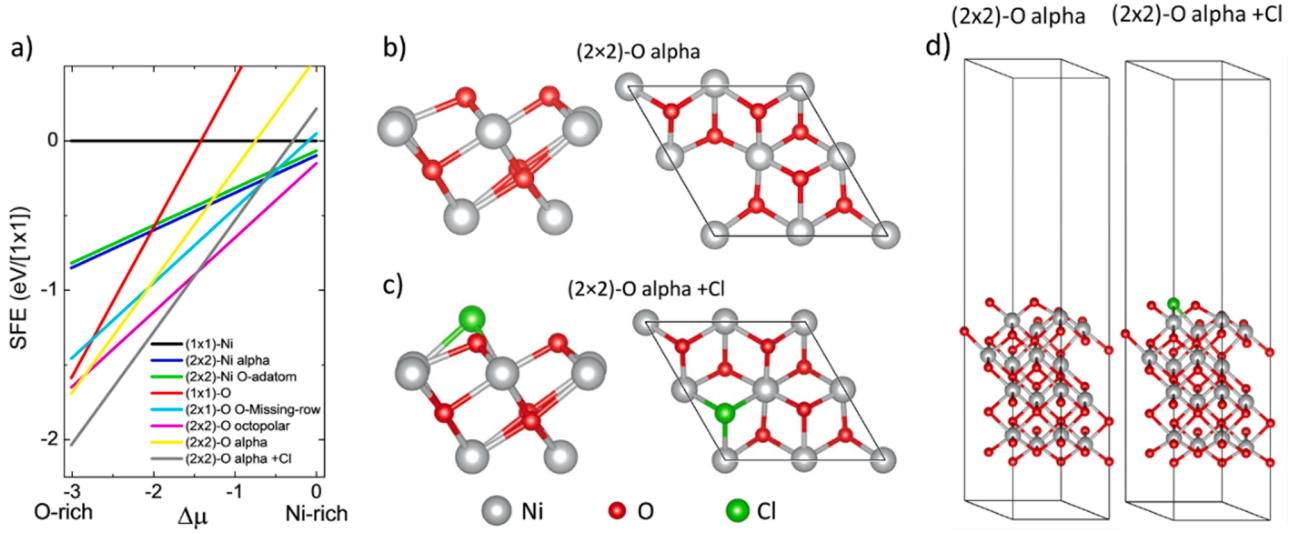

Fig. 4. (a) SFE plot vs. the chemical potential for different NiO (111) surface reconstructions. (b) O-alpha model, (c) O-alpha model with a Cl atom filling the vacancy, (d) side view of the model system.

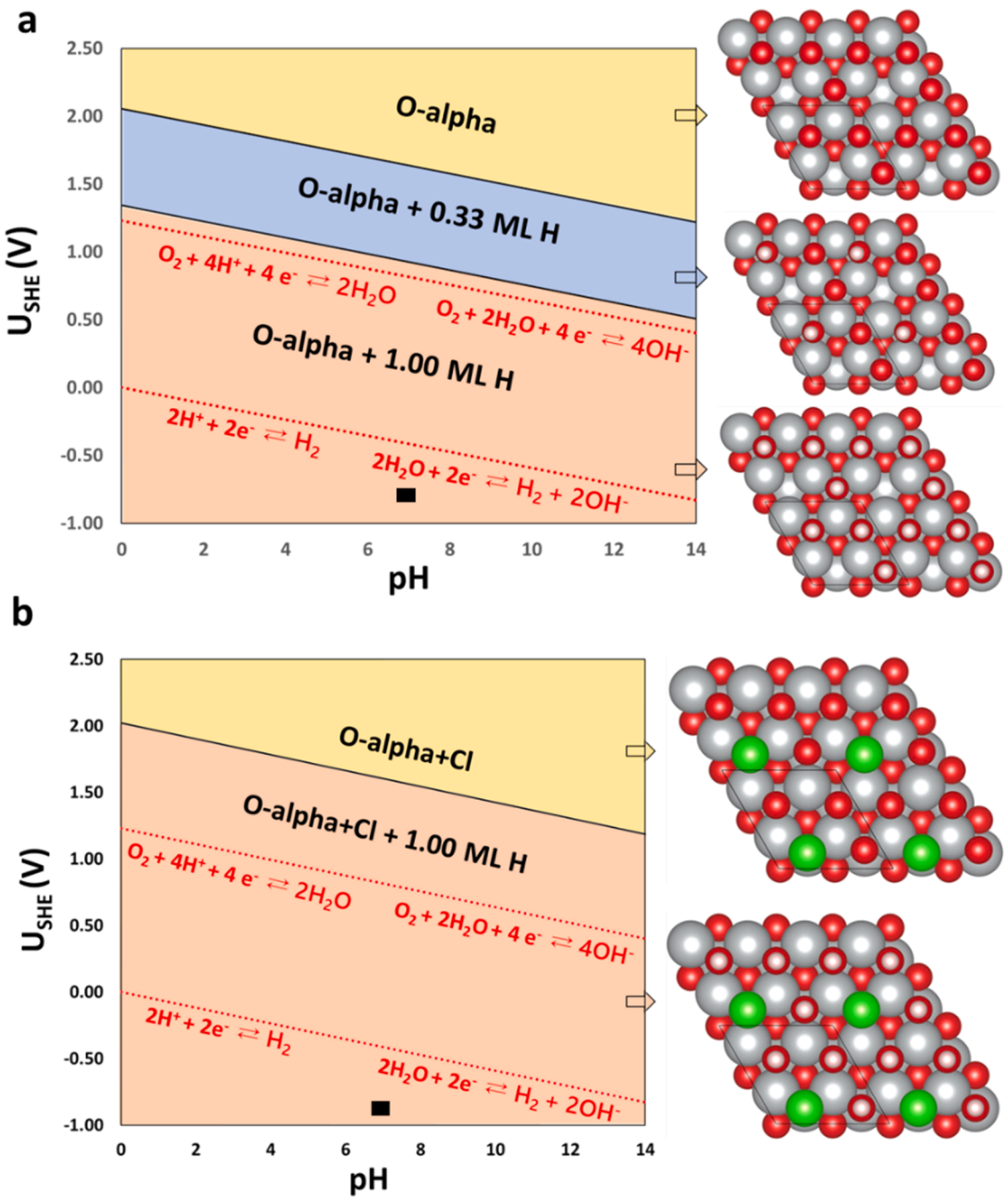

Fig. 5. Surface Pourbaix diagram derived from DFT of thermodynamically stable hydrogenations on (a) O-alpha and (b) O-alpha with chlorine atom doped model. The color code in our model is grey for Ni, red for O, green for Cl, and red for H. The black boxes indicate the optimal experimental conditions (U=-0.8(± 0.05)V and pH=6.8(± 0.2) used in this work.

required for oxygen reduction and hydrogen evolution reactions indicted in dashed lines. Furthermore, H_2O and NiH_X formation might be possible in the area of the Pourbaix diagram where H_2 is produced.

The Pourbaix diagram for the NiO O-alpha vacancy with Cl is presented in Fig. 5**b**. The vacant site generated by removing oxygen from oxygen terminated nickel oxide (O-alpha) is occupied with a chlorine atom (O-alpha+Cl). The surface is thermally stable surfaces upon H adsorption at varied pH and potential. The non-hydrogenated clean surface is most stable beyond 2.02 V at acidic conditions, while at pH=14, the range reduces up to 1.19 V. Interestingly, with a decrease in potential, hydrogenation over the clean surface is highly favored, leading to adsorption of 1.00 ML of H atoms in the potential range of 2.02 to -1 V at pH=0. The observations from Fig. 5**a** and **b** clearly indicate the stability of chlorine-containing O-alpha surface compared to the bare O-alpha upon hydrogenation.

An effective catalyst should be highly stable at U_{SHE}=0. Thus we examined the stability of these hydrogenated surfaces with and without chlorine as a function of pH at U_{SHE} of 0 [83]. In **Fig. S23**, the bottom line corresponds to 1.00 ML of H terminated O-alpha+Cl state. The results demonstrate the stability acquired by O-alpha model upon incorporating Cl atoms in its vacant site. The hydrogenated O-alpha and O-alpha+Cl surfaces are favorable at experimental conditions of U = -0.8 and pH=6.8 (highlighted with a black square in Fig. 5). It might be plausible that the local pH at the electrode might further increase during the reaction. O-alpha+Cl surface remains favorable over a wide pH range.

The stability of the O-alpha+Cl is demonstrated in Figs. 4 and 5; further mechanistic insights for CO_2RR are generated for O-alpha and O-alpha+Cl in NiO. Since the oxygen atoms of the surface are very reactive and the surface is exposed to hydrogen protons, the oxygen atoms of the substrate are passivated by hydrogen atoms. Therefore, hydrogenated surfaces at the initial step of the reaction are used. The energetics and geometries of some particular states are studied to describe the CO_2 reduction reaction in the substrate without Cl (Fig. 6). This includes (*i*) the initial state in which the molecule and the substrate are not interacting (**ZS**), (ii) the state in which the CO_2 molecule is physisorbed (we call it the intermediate state or **IS**), (iii) the final state in which the formate is formed after abstracting an H atom, and it is chemisorbed in the oxygen vacancy of the substrate (final state 1 **FS1**), and the second final state in which the formate and the substrate are not interacting (final state or **FS2**). The minimum energy path is calculated to consider the kinetics of the reaction. As shown in Fig. 6**a, b** for NiO, there is an increase in the energy of 0.26 eV, going from **ZS** to **IS**. In fact, there is no energy barrier to arrive at this intermediate state. As the reaction evolves, a hydrogen atom from the environment has to bond with the molecule carbon atom, forming an adsorbed formate on the surface (**FS1**). In this case, there is an energy barrier (call transition state or **TS**) of 0.19 eV, and the system gains 3.58 eV in energy. However, a large energy barrier of 3.93 eV allows the formate to desorb and reach **FS2**. Therefore, it prefers to stay on the surface, and our calculations clearly explain why we do not observe formate in our experiments as in the case of NiO@Cl-1% (low Cl), NiO@Red (low Cl), and commercial NiO (no Cl) in Fig. 3**b**. Once on the substrate, the formate may react with other atoms or molecules to form other compounds (we did not further investigate all possibilities) [84]. However, insights on CO_2 reduction to CO are discussed below.

The minimum energy path for the CO_2RR in the presence of chlorine is studied, as shown in Fig. 6**a** and **c**. The situation is now different since Cl atoms occupy the oxygen vacancies. In this case, the CO_2 molecule is physisorbed on top of the Cl atom, gaining 0.22 eV (**IS**). To show how Cl interacts with the CO_2 molecule to promote its electroreduction, the non-covalent interaction index (NCI) between chlorinated surfaces and the CO_2 molecule is plotted in **Fig. S24**. It has been found that the primary interaction of the molecule is with the O-alpha+Cl in NiO. To continue with the reaction, a hydrogen atom from the environment has to form a bond with the carbon atom of the molecule, resulting in a formation of physisorbed formate on the surface. This reaction step shows a very small energy barrier (**TS**) of 0.05 eV, and the system gains 0.86 eV (**FS1**). To desorb formate from the surface, 0.96 eV (**FS2**) is needed, much smaller than 3.93 eV without chlorine. These results explain why we have experimentally observed formate in NiO@Cl-9%, i.e., the sample with more Cl present (Table 1). This sample also has the highest Ni^{3+}/Ni^{2+} suggesting the presence of defects, such as oxygen vacancies (Fig. 4). The energy barrier for the formation of formate without the substrate is 0.31 eV, demonstrating the importance of the Cl-filled vacancies in the NiO surface. In addition to the CO_2RR to formate on the chlorinated NiO surfaces, CO formation is considered. CO is obtained through the reaction: $CO_2 + H_2 \rightarrow CO + H_2O$. The first reaction step occurs when an H atom of the medium interacts with the O of the CO_2 molecule. However, this configuration is less stable (by 0.45 eV). Therefore, since the CO formation is energetically less favorable (**Fig. S25**), we only focus on the CO_2 to formate pathway.

4. Conclusion

Cl containing NiO octahedra are synthesized using a solid-state method. The NiO functionality is demonstrated during CO_2RR, yielding to a $FE_{HCOO-} = 70\%$, $FE_{H2} = 15\%$, and $FE_{CO} = 3\%$, at -0.8 V vs.

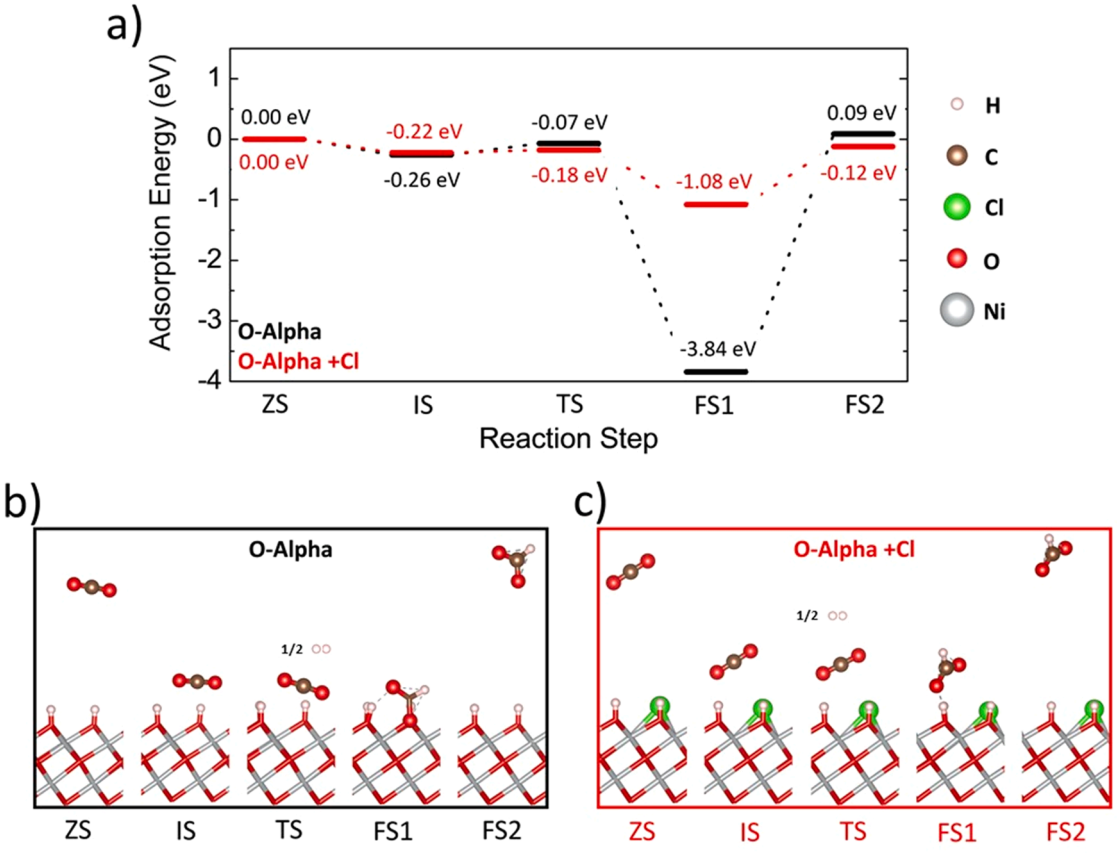

Fig. 6. (a) DFT calculations of the energetics of the optimized reaction coordinate for the reduction of CO_2 into formate on the O-alpha surface (b) in the absence of Cl (black) and (c) with Cl (red).

RHE with a total current density of -21 mA/cm^2 over 4 h operation. Over longer-term operation (i.e., 24 h), the FE to formate lowers to ca. 63%, and the amount of H_2 and CO production remains close to 20 and 6.5% with nearly no changes in the total current density. XPS confirms the presence of Ni^{2+} and Ni^{3+} species in the NiO, and with increasing Cl concentration, the Ni^{3+}/Ni^{2+} ratio also increases. It is found that Cl plays a key role in introducing Ni^{3+} species. DFT is used to provide insights into the reaction mechanism by comparing NiO and chloride-containing NiO. It is found that Cl can occupy defect sites, such as oxygen alpha vacancies, thereby aiding in the promotion of CO_2RR to the selective production formate over CO. The results are the first attempt toward chlorine-mediated defect engineering in NiO for selective formate production. From a broader perspective, our work opens up new possibilities for the next generation of halogenated catalysts for CO_2R.

CRediT authorship contribution statement

M.A. Rodriguez-Olguin: Investigation, Formal analysis, Writing – original draft, Writing – review & editing. **C. Flox:** Investigation, Formal analysis, Writing – original draft, Writing – review & editing. **R. Ponce-Pérez:** Investigation, Writing – review & editing. **R. Lipin:** Investigation, Methodology, Writing – review & editing. **F. Ruiz-Zepeda:** Formal analysis, Writing – review & editing. **J.P. Winczewski:** Investigation, Writing – review & editing. **T. Kallio:** Visualization, Writing – review & editing. **M. Vandichel:** Investigation, Methodology, Visualization, Writing – review & editing. **J. Guerrero-Sánchez:** Investigation, Writing – review & editing. **J.G.E. Gardeniers:** Visualization, Writing – review & editing. **N. Takeuchi:** Investigation, Writing – review & editing. **A. Susarrey-Arce:** Investigation, Formal analysis, Writing – original draft, Visualization, Project administration, Writing – review & editing.

Declaration of Competing Interest

The authors declare no competing interests.

Acknowledgments

The authors thank Mark Smithers and Gerard Kip (MESA+ Institute, University of Twente) for their support. The research leading to this report's results has received funding from the European Research Council (ERC) under the European Union's Horizon 2020 research and innovation program (Grant agreement No. 742004). We also thank DGAPA-UNAM projects IN105722, IA100920, IN110820 and CONACyT grant A1-S-9070, for partial financial support. Calculations were performed in the DGCTIC-UNAM Supercomputing Center, projects LANCAD-UNAM-DGTIC-051, LANCAD-UNAM-DGTIC-368 and LANCAD-UNAM-DGTIC-150. R.P.P. acknowledges CONACyT for the postdoctoral position. F.R.-Z would like to acknowledge the Slovenian Research Agency program P2-0393. R.L. and M.V. acknowledge the Irish Centre for High-End Computing (ICHEC) for the computational facilities and support

Supplementary materials

Supplementary material associated with this article can be found, in the online version, at doi:10.1016/j.apmt.2022.101528.

References

[1] C. Le Quéré, R.B. Jackson, M.W. Jones, A.J.P. Smith, S. Abernethy, R.M. Andrew, A.J. De-Gol, D.R. Willis, Y. Shan, J.G. Canadell, P. Friedlingstein, F. Creutzig, G. P. Peters, Temporary reduction in daily global CO2 emissions during the COVID-19 forced confinement, Nat. Clim. Change 10 (2020) 647–653, https://doi.org/10.1038/s41558-020-0797-x.

[2] A. Manne, R. Richels, US rejection of the kyoto protocol: the impact on compliance costs and CO_2 emissions, Energy Policy 32 (2004) 447–454, https://doi.org/10.1016/S0301-4215(03)00147-2.

[3] C. Acar, I. Dincer, Comparative assessment of hydrogen production methods from renewable and non-renewable sources, Int. J. Hydrog. Energy 39 (2014) 1–12, https://doi.org/10.1016/j.ijhydene.2013.10.060.

[4] T. Kim, G.T.R. Palmore, A scalable method for preparing Cu electrocatalysts that convert CO_2 into C_{2+} products, Nat. Commun. 111 (11) (2020) 1–11, https://doi.org/10.1038/s41467-020-16998-9, 2020.

[5] Y. Wang, P. Han, X. Lv, L. Zhang, G. Zheng, Defect and interface engineering for aqueous electrocatalytic CO_2 reduction, Joule 2 (2018) 2551–2582, https://doi.org/10.1016/j.joule.2018.09.021.

[6] Z. Yin, G.T.R. Palmore, S. Sun, Electrochemical reduction of CO_2 catalyzed by metal nanocatalysts, Trends Chem. 1 (2019) 739–750, https://doi.org/10.1016/j.trechm.2019.05.004.

[7] R. Ma, Y.L. Chen, Y. Shen, H. Wang, W. Zhang, S.S. Pang, J. Huang, Y. Han, Y. Zhao, Anodic SnO_2porous nanostructures with rich grain boundaries for efficient CO_2electroreduction to formate, RSC Adv. 10 (2020) 22828–22835, https://doi.org/10.1039/d0ra03152f.

[8] D. Gao, F. Scholten, B. Roldan Cuenya, Improved CO_2 electroreduction performance on plasma-activated Cu catalysts via electrolyte design: halide effect, ACS Catal. 7 (2017) 5112–5120, https://doi.org/10.1021/acscatal.7b01416.

[9] M. Li, Y. Ma, J. Chen, R. Lawrence, W. Luo, M. Sacchi, W. Jiang, J. Yang, Residual chlorine induced cationic active species on a porous copper electrocatalyst for highly stable electrochemical CO_2 reduction to C_{2+}, Angew. Chem. Int. Ed. 60 (2021) 11487–11493, https://doi.org/10.1002/anie.202102606.

[10] A. Goyal, G. Marcandalli, V.A. Mints, M.T.M. Koper, Competition between CO_2reduction and hydrogen evolution on a gold electrode under well-defined mass transport conditions, J. Am. Chem. Soc. 142 (2020) 4154–4161, https://doi.org/10.1021/jacs.9b10061.

[11] E.R. Cave, C. Shi, K.P. Kuhl, T. Hatsukade, D.N. Abram, C. Hahn, K. Chan, T. F. Jaramillo, Trends in the catalytic activity of hydrogen evolution during CO_2 electroreduction on transition metals, ACS Catal. 8 (2018) 3035–3040, https://doi.org/10.1021/acscatal.7b03807.

[12] M. Zhao, H. Tang, Q. Yang, Y. Gu, H. Zhu, S. Yan, Z. Zou, Inhibiting hydrogen evolution using a chloride adlayer for efficient electrochemical CO_2 reduction on Zn electrodes, ACS Appl. Mater. Interfaces 12 (2020) 4565–4571, https://doi.org/10.1021/acsami.9b22811.

[13] Y.J. Sa, C.W. Lee, S.Y. Lee, J. Na, U. Lee, Y.J. Hwang, Catalyst-electrolyte interface chemistry for electrochemical CO_2reduction, Chem. Soc. Rev. 49 (2020) 6632–6665, https://doi.org/10.1039/d0cs00030b.

[14] W. Ni, Y. Xue, X. Zang, C. Li, H. Wang, Z. Yang, Y.M. Yan, Fluorine doped cagelike carbon electrocatalyst: an insight into the structure-enhanced CO selectivity for CO_2 reduction at high overpotential, ACS Nano 14 (2020) 2014–2023, https://doi.org/10.1021/acsnano.9b08528.

[15] H. Yang, Q. Lin, C. Zhang, X. Yu, Z. Cheng, G. Li, Q. Hu, X. Ren, Q. Zhang, J. Liu, C. He, Carbon dioxide electroreduction on single-atom nickel decorated carbon membranes with industry compatible current densities, Nat. Commun. 11 (2020) 593, https://doi.org/10.1038/s41467-020-14402-0.

[16] S. Hernández, M.A. Farkhondehfal, F. Sastre, M. Makkee, G. Saracco, N. Russo, Syngas production from electrochemical reduction of CO_2: current status and prospective implementation, Green Chem. 19 (2017) 2326–2346, https://doi.org/10.1039/c7gc00398f.

[17] G. Peng, S.J. Sibener, G.C. Schatz, S.T. Ceyer, M. Mavrikakis, CO_2 hydrogenation to formic acid on Ni(111), J. Phys. Chem. C 116 (2012) 3001–3006, https://doi.org/10.1021/jp210408x.

[18] A. Kudo, S. Nakagawa, A. Tsuneto, T. Sakata, Electrochemical reduction of high pressure CO_2 on Ni electrodes, J. Electrochem. Soc. 140 (1993) 1541–1545, https://doi.org/10.1149/1.2221599.

[19] Z. Zhao, Z. Chen, G. Lu, Computational discovery of nickel-based catalysts for CO_2 reduction to formic acid, J. Phys. Chem. C 121 (2017) 20865–20870, https://doi.org/10.1021/acs.jpcc.7b06895.

[20] X.J. He, J.X. Feng, Q. Ren, G.R. Li, Ni nanoparticle-decorated-MnO_2 nanodendrites as highly selective and efficient catalysts for CO_2 electroreduction, J. Mater. Chem. A 6 (2018) 19438–19444, https://doi.org/10.1039/c8ta07687a.

[21] E.L. Clark, J. Resasco, A. Landers, J. Lin, L.T. Chung, A. Walton, C. Hahn, T. F. Jaramillo, A.T. Bell, Standards and protocols for data acquisition and reporting for studies of the electrochemical reduction of carbon dioxide, ACS Catal. 8 (2018) 6560–6570, https://doi.org/10.1021/acscatal.8b01340.

[22] X. Zhang, X. Du, Oxygen vacancies confined in nickel oxide nanoprism arrays for promoted electrocatalytic water splitting, New J. Chem. 44 (2020) 1703–1706, https://doi.org/10.1039/C9NJ05940G.

[23] Z. Lin, C. Du, B. Yan, C. Wang, G. Yang, Two-dimensional amorphous NiO as a plasmonic photocatalyst for solar H_2 evolution, Nat. Commun. 91 (9) (2018) 1–11, https://doi.org/10.1038/s41467-018-06456-y, 2018.

[24] M. Shen, L. Zhang, J. Shi, Defect engineering of photocatalysts towards elevated CO_2 reduction performance, ChemSusChem 14 (2021) 2635–2654, https://doi.org/10.1002/CSSC.202100677.

[25] E. Arciga-Duran, Y. Meas, J.J. Pérez-Bueno, J.C. Ballesteros, G. Trejo, Effect of oxygen vacancies in electrodeposited NiO towards the oxygen evolution reaction: role of Ni-Glycine complexes, Electrochim. Acta 268 (2018) 49–58, https://doi.org/10.1016/j.electacta.2018.02.099.

[26] J. Bao, X. Zhang, B. Fan, J. Zhang, M. Zhou, W. Yang, X. Hu, H. Wang, B. Pan, Y. Xie, Ultrathin spinel-structured nanosheets rich in oxygen deficiencies for enhanced electrocatalytic water oxidation, Angew. Chem. 127 (2015) 7507–7512, https://doi.org/10.1002/ange.201502226.

[27] T. Zhang, M.Y. Wu, D.Y. Yan, J. Mao, H. Liu, W. Bin Hu, X.W. Du, T. Ling, S. Z. Qiao, Engineering oxygen vacancy on NiO nanorod arrays for alkaline hydrogen evolution, Nano Energy 43 (2018) 103–109, https://doi.org/10.1016/j.nanoen.2017.11.015.

[28] B. Liu, H. Yang, A. Wei, H. Zhao, L. Ning, C. Zhang, S. Liu, Superior photocatalytic activities of NiO octahedrons with loaded AgCl particles and charge separation between polar NiO {111} surfaces, Appl. Catal. B Environ. 172-173 (2015) 165–173, https://doi.org/10.1016/j.apcatb.2015.02.007.

[29] Y. Lv, K. Huang, W. Zhang, S. Ran, F. Chi, B. Yang, X. Liu, High-performance gas-sensing properties of octahedral NiO crystals prepared via one-step controllable synthesis route, Cryst. Res. Technol. 49 (2014) 109–115, https://doi.org/10.1002/crat.201300309.

[30] Y. Ye, Y. Zhao, L. Ni, K. Jiang, G. Tong, Y. Zhao, B. Teng, Facile synthesis of unique NiO nanostructures for efficiently catalytic conversion of CH_4 at low temperature, Appl. Surf. Sci. 362 (2016) 20–27, https://doi.org/10.1016/j.apsusc.2015.11.213.

[31] W. Cai, S. Zhang, J. Lv, J. Chen, J. Yang, Y. Wang, X. Guo, L. Peng, W. Ding, Y. Chen, Y. Lei, Z. Chen, W. Yang, Z. Xie, Nanotubular gamma alumina with high-energy external surfaces: synthesis and high performance for catalysis, ACS Catal. 7 (2017) 4083–4092, https://doi.org/10.1021/acscatal.7b00080.

[32] W. Zhou, M. Zhou, J. Hu, H. Dong, Y. Ou, L. Yang, X. Wei, P. Xiao, Y. Zhang, Shape-controlled synthesis of Ni nanocrystals: via a wet-chemistry strategy and their shape-dependent catalytic activity, CrystEngComm 21 (2019) 1416–1422, https://doi.org/10.1039/c8ce01915k.

[33] B. Liu, M. Wang, S. Liu, H. Zheng, H. Yang, The sensing reaction on the Ni-NiO (111) surface at atomic and molecule level and migration of electron, Sen. Actuators B Chem. 273 (2018) 794–803, https://doi.org/10.1016/j.snb.2018.06.102.

[34] X.Y. Yu, L. Yu, H. Bin Wu, X.W. Lou, Formation of nickel sulfide nanoframes from metal-organic frameworks with enhanced pseudocapacitive and electrocatalytic properties, Angew. Chem. Int. Ed. 54 (2015) 5331–5335, https://doi.org/10.1002/anie.201500267.

[35] Y. Liu, C. Gao, Q. Li, H. Pang, Nickel oxide/graphene composites: synthesis and applications, Chem. A Eur. J. 25 (2019) 2141–2160, https://doi.org/10.1002/chem.201803982.

[36] G. Kresse, J. Hafner, Ab initio molecular dynamics for liquid metals, Phys. Rev. B 47 (1993) 558–561, https://doi.org/10.1103/PhysRevB.47.558.

[37] G. Kresse, J. Hafner, Ab initio molecular-dynamics simulation of the liquid-metalamorphous- semiconductor transition in germanium, Phys. Rev. B 49 (1994) 14251–14269, https://doi.org/10.1103/PhysRevB.49.14251.

[38] G. Kresse, J. Furthmüller, Efficiency of ab-initio total energy calculations for metals and semiconductors using a plane-wave basis set, Comput. Mater. Sci. 6 (1996) 15–50, https://doi.org/10.1016/0927-0256(96)00008-0.

[39] G. Kresse, J. Furthmüller, Efficient iterative schemes for ab initio total-energy calculations using a plane-wave basis set, Phys. Rev. B Condens. Matter Mater. Phys. 54 (1996) 11169–11186, https://doi.org/10.1103/PhysRevB.54.11169.

[40] J.P. Perdew, K. Burke, M. Ernzerhof, Generalized gradient approximation made simple, Phys. Rev. Lett. 77 (1996) 3865–3868, https://doi.org/10.1103/PhysRevLett.77.3865.

[41] V.I. Anisimov, F. Aryasetiawan, A.I. Lichtenstein, First-principles calculations of the electronic structure and spectra of strongly correlated systems: the LDA + U method, J. Phys. Condens. Matter 9 (1997) 767–808, https://doi.org/10.1088/0953-8984/9/4/002.

[42] G. Peng, L.R. Merte, J. Knudsen, R.T. Vang, E. Lægsgaard, F. Besenbacher, M. Mavrikakis, On the mechanism of low-temperature CO oxidation on Ni(111) and NiO(111) surfaces, J. Phys. Chem. C 114 (2010) 21579–21584, https://doi.org/10.1021/jp108475e.

[43] W.B. Zhang, B.Y. Tang, Stability of the polar NiO(111) surface, J. Chem. Phys. (2008) 128, https://doi.org/10.1063/1.2835544.

[44] P.E. Blöchl, Projector augmented-wave method, Phys. Rev. B 50 (1994) 17953–17979, https://doi.org/10.1103/PhysRevB.50.17953.

[45] D. Joubert, From ultrasoft pseudopotentials to the projector augmented-wave method, Phys. Rev. B Condens. Matter Mater. Phys. 59 (1999) 1758–1775, https://doi.org/10.1103/PhysRevB.59.1758.

[46] S. Grimme, J. Antony, S. Ehrlich, H. Krieg, A consistent and accurate ab initio parametrization of density functional dispersion correction (DFT-D) for the 94 elements H-Pu, J. Chem. Phys. (2010) 132, https://doi.org/10.1063/1.3382344.

[47] S. Grimme, S. Ehrlich, L. Goerigk, Effect of the damping function in dispersion corrected density functional theory, J. Comput. Chem. 32 (2011) 1456–1465, https://doi.org/10.1002/jcc.21759.

[48] H.J. Monkhorst, J.D. Pack, Special points for brillouin-zone integrations, Phys. Rev. B. 13 (1976) 5188–5192, https://doi.org/10.1103/PhysRevB.13.5188.

[49] N. Takeuchi, S.E. Ulloa, First-principles calculations of the structural and electronic properties of the ScN(001) surface, Phys. Rev. B Condens. Matter Mater. Phys. 65 (2002) 2353071–2353075, https://doi.org/10.1103/PhysRevB.65.235307.

[50] N. Takeuchi, Surface properties of YN(001): a first-principles calculation, Phys. Rev. B Condens. Matter Mater. Phys. 66 (2002) 1–3, https://doi.org/10.1103/PhysRevB.66.153405.

[51] G.X. Qian, R.M. Martin, D.J. Chadi, First-principles study of the atomic reconstructions and energies of Ga- and As-stabilized GaAs(100) surfaces, Phys. Rev. B 38 (1988) 7649–7663, https://doi.org/10.1103/PhysRevB.38.7649.

[52] R. Ponce-Pérez, K. Alam, G.H. Cocoletzi, N. Takeuchi, A.R. Smith, Structural, electronic, and magnetic properties of the CrN (0 0 1) surface: first-principles studies, Appl. Surf. Sci. 454 (2018) 350–357, https://doi.org/10.1016/j.apsusc.2018.05.118.

[53] A.C. Martínez-Olguín, R. Ponce-Pérez, C.A. Corona-García, D.M. Hoat, L.M. de la Garza, M.G. Moreno-Armenta, G.H. Cocoletzi, Theoretical investigation of the AlN (0 0 0 1)-(2 × 2) surface doped with nickel: structural, electronic and magnetic properties, J. Cryst. Growth (2020) 551, https://doi.org/10.1016/j.jcrysgro.2020.125907.

[54] Q. Fu, M. Ai, Y. Duan, L. Lu, X. Tian, D. Sun, Y. Xu, Y. Sun, Synthesis of uniform porous NiO nanotetrahedra and their excellent gas-sensing performance toward formaldehyde, RSC Adv. 7 (2017) 52312–52320, https://doi.org/10.1039/c7ra10730g.

[55] M. Taeño, J. Bartolomé, L. Gregoratti, P. Modrzynski, D. Maestre, A. Cremades, Self-organized NiO microcavity arrays fabricated by thermal treatments, Cryst. Growth Des. 20 (2020) 4082–4091, https://doi.org/10.1021/acs.cgd.0c00365.

[56] G. Zhang, Y. Chen, B. Qu, L. Hu, L. Mei, D. Lei, Q. Li, L. Chen, Q. Li, T. Wang, Synthesis of mesoporous NiO nanospheres as anode materials for lithium ion batteries, Electrochim. Acta 80 (2012) 140–147, https://doi.org/10.1016/j.electacta.2012.06.107.

[57] A.N. Mansour, Characterization of NiO by XPS, Surf. Sci. Spectra 3 (1994) 231–238, https://doi.org/10.1116/1.1247751.

[58] J.H. Li, C.C. Wang, C.J. Huang, Y.F. Sun, W.Z. Weng, H.L. Wan, Mesoporous nickel oxides as effective catalysts for oxidative dehydrogenation of propane to propene, Appl. Catal. A Gen. 382 (2010) 99–105, https://doi.org/10.1016/j.apcata.2010.04.034.

[59] X. Xu, L. Li, J. Huang, H. Jin, X. Fang, W. Liu, N. Zhang, H. Wang, X. Wang, Engineering Ni^{3+} cations in NiO lattice at the atomic level by Li^{+} doping: the roles of Ni^{3+} and oxygen species for CO oxidation, ACS Catal. 8 (2018) 8033–8045, https://doi.org/10.1021/acscatal.8b01692.

[60] S. Uhlenbrock, C. Scharfschwerdt, M. Neumann, G. Illing, H.J. Freund, The influence of defects on the Ni 2p and O 1s XPS of NiO, J. Phys. Condens. Matter 4 (1992) 7973–7978, https://doi.org/10.1088/0953-8984/4/40/009.

[61] X. Xu, H. Zhang, Y. Tong, Y. Sun, X. Fang, J. Xu, X. Wang, Tuning Ni3+ quantity of NiO via doping of cations with varied valence states: the key role of Ni^{3+} on the reactivity, Appl. Surf. Sci. 550 (2021), 149316, https://doi.org/10.1016/j.apsusc.2021.149316.

[62] C.N.R. Rao, V. Vijayakrishnan, G.U. Kulkarni, M.K. Rajumon, A comparative study of the interaction of oxygen with clusters and single-crystal surfaces of nickel, Appl. Surf. Sci. 84 (1995) 285–289, https://doi.org/10.1016/0169-4332(94)00548-6.

[63] P. Salunkhe, A.V. Muhammed Ali, D. Kekuda, Investigation on tailoring physical properties of nickel oxide thin films grown by dc magnetron sputtering, Mater. Res. Express 7 (2020), 016427, https://doi.org/10.1088/2053-1591/AB69C5.

[64] J.K. Kim, PEG-assisted sol-gel synthesis of compact nickel oxide hole-selective layer with modified interfacial properties for organic solar cells, Polymers 11 (2019), https://doi.org/10.3390/polym11010120 (Basel).

[65] A.Y. Faid, A.O. Barnett, F. Seland, S. Sunde, Ni/NiO nanosheets for alkaline hydrogen evolution reaction: *in situ* electrochemical-Raman study, Electrochim. Acta 361 (2020), 137040, https://doi.org/10.1016/J.ELECTACTA.2020.137040.

[66] S. Liu, R. Liu, Y. Chen, S. Ho, J.H. Kim, F. So, Nickel oxide hole injection/transport layers for efficient solution-processed organic light-emitting diodes, Chem. Mater. 26 (2014) 4528–4534, https://doi.org/10.1021/cm501898y.

[67] M.C. Biesinger, L.W.M. Lau, A.R. Gerson, R.S.C. Smart, The role of the Auger parameter in XPS studies of nickel metal, halides and oxides, Phys. Chem. Chem. Phys. 14 (2012) 2434–2442, https://doi.org/10.1039/c2cp22419d.

[68] Z. Chen, T. Dedova, I.O. Acik, M. Danilson, M. Krunks, Nickel oxide films by chemical spray: effect of deposition temperature and solvent type on structural, optical, and surface properties, Appl. Surf. Sci. 548 (2021), 149118, https://doi.org/10.1016/j.apsusc.2021.149118.

[69] N. Kumar, H.B. Lee, S. Hwang, J.W. Kang, Large-area, green solvent spray deposited nickel oxide films for scalable fabrication of triple-cation perovskite solar cells, J. Mater. Chem. A 8 (2020) 3357–3368, https://doi.org/10.1039/c9ta13528f.

[70] M. Cui, X. Ding, X. Huang, Z. Shen, T.L. Lee, F.E. Oropeza, J.P. Hofmann, E.J. M. Hensen, K.H.L. Zhang, Ni^{3+}-induced hole states enhance the oxygen evolution reaction activity of $NixCo_{3-x}O_4$ electrocatalysts, Chem. Mater. 31 (2019) 7618–7625, https://doi.org/10.1021/acs.chemmater.9b02453.

[71] C.A. Tolman, W.M. Riggs, W.J. Linn, C.M. King, R.C. Wendt, Electron spectroscopy for chemical analysis of nickel compounds, Inorg. Chem. 12 (1973) 2770–2778, https://doi.org/10.1021/ic50130a006.

[72] W.E. Morgan, J.R. Van Wazer, W.J. Stec, Inner-orbital photoelectron spectroscopy of the alkali metal halides, perchlorates, phosphates, and pyrophosphates, J. Am. Chem. Soc. 95 (1973) 751–755, https://doi.org/10.1021/ja00784a018.

[73] G.E. Wagner, C.D. Briggs, W.M. Davis, L.E. Moulder, J.F. Muilenberg, Handbook of X-ray photoelectron spectroscopy. Handb. X-Ray Photoelectron Spectroscopy, Perkin Elmer Corp, Physical Electronics Division, 1992.

[74] C.T. Dinh, T. Burdyny, G. Kibria, A. Seifitokaldani, C.M. Gabardo, F. Pelayo García De Arquer, A. Kiani, J.P. Edwards, P. De Luna, O.S. Bushuyev, C. Zou, R. Quintero-Bermudez, Y. Pang, D. Sinton, E.H. Sargent, CO_2 electroreduction to ethylene via hydroxide-mediated copper catalysis at an abrupt interface, Science 360 (80) (2018) 783–787, https://doi.org/10.1126/science.aas9100.

[75] H. Pan, C.J. Barile, Electrochemical CO_2 reduction to methane with remarkably high Faradaic efficiency in the presence of a proton permeable membrane, Energy Environ. Sci. 13 (2020) 3567–3578, https://doi.org/10.1039/d0ee02189j.

[76] S. Ikeda, A. Hattori, M. Maeda, K. Ito, H. Noda, Electrochemical reduction behavior of carbon dioxide on sintered zinc oxide electrode in aqueous solution, Electrochemistry 68 (2000) 257–261, https://doi.org/10.5796/electrochemistry.68.257.

[77] M. Fan, C. Ma, T. Lei, J. Jung, D. Guay, J. Qiao, Aqueous-phase electrochemical reduction of CO_2 based on SnO_2–CuO nanocomposites with improved catalytic

activity and selectivity, Catal. Today 318 (2018) 2–9, https://doi.org/10.1016/j.cattod.2017.09.018.
[78] F. Finocchi, A. Barbier, J. Jupille, C. Noguera, Stability of Rocksalt (111) polar surfaces: beyond the octopole, Phys. Rev. Lett. 92 (2004) 2–5, https://doi.org/10.1103/PhysRevLett.92.136101.
[79] A. Barbier, C. Mocuta, H. Kuhlenbeck, K.F. Peters, B. Richter, G. Renaud, Atomic structure of the polar NiO(111)-p(2 × 2) surface, Phys. Rev. Lett. 84 (2000) 2897–2900, https://doi.org/10.1103/PhysRevLett.84.2897.
[80] T.C. Chang, Y.T. Lu, C.H. Lee, J.K. Gupta, L.J. Hardwick, C.C. Hu, H.Y.T. Chen, The effect of degrees of inversion on the electronic structure of spinel $NiCo_2O_4$: a density functional theory study, ACS Omega 6 (2021) 9692–9699, https://doi.org/10.1021/acsomega.1c00295.
[81] H.A. Hansen, J. Rossmeisl, J.K. Nørskov, Surface Pourbaix diagrams and oxygen reduction activity of Pt, Ag and Ni(111) surfaces studied by DFT, Phys. Chem. Chem. Phys. 10 (2008) 3722–3730, https://doi.org/10.1039/B803956A.
[82] D. Kramer, Y. Wang, J. Wharton, Mechano-electrochemistry effects due to deformation of copper oxide films, Faraday Discuss. 180 (2015) 137–149, https://doi.org/10.1039/C4FD00247D.
[83] J. Gan, F. Li, Y. Tang, Q. Tang, Theoretical study of transition-metal-modified Mo_2CO_2 MXene as a catalyst for the hydrogen evolution reaction, ChemSusChem 13 (2020) 6005–6015, https://doi.org/10.1002/CSSC.202002163.
[84] J. Hussain, H. Jónsson, E. Skúlason, Calculations of product selectivity in electrochemical CO_2 reduction, ACS Catal. 8 (2018) 5240–5249, https://doi.org/10.1021/acscatal.7b03308.